Journal of
Materials Chemistry C

PAPER

View Article Online
View Journal | View Issue

Cite this: *J. Mater. Chem. C*, 2025, **13**, 15655

Improving the current stability of perovskite quantum dot phototransistors utilizing the ferrocene–cyclodextrin host–guest supramolecules as a floating gate dielectric†

Yi-Wen Chen,[a] Ya-Shuan Wu,[b] Ender Ercan,[c] Takuya Isono,[d] Toshifumi Satoh,[def] Cheng-Liang Liu,[gh] Yan-Cheng Lin,*[hi] Chen-Tsyr Lo*[a] and Wen-Chang Chen*[bh]

Received 23rd April 2025,
Accepted 18th June 2025

DOI: 10.1039/d5tc01629k

rsc.li/materials-c

Photodetectors have garnered significant attention due to their vital role in a wide range of applications, including optical communication, environmental monitoring, and imaging technologies. However, the design and optimization of high-performance photodetector materials remain an ongoing challenge. In this study, a novel electroactive supramolecular floating-gate layer is developed by utilizing host–guest interactions between β-cyclodextrin (β-CD) and ferrocene. This supramolecular structure is integrated into a phototransistor as the floating gate dielectric to enhance photoresponse capabilities, facilitating rapid photoresponse due to its efficient charge transport properties, which minimize charge accumulation. Furthermore, the incorporation of perovskite quantum dots (QDs) enhances the device's optical response. With the optimal supramolecular composition of 5 wt% β-CD-modified QDs in the ferrocene-functionalized polymer to form host–guest supramolecules, the transient photocurrent response confirms its superior performance, with shorter rise and fall times (0.18 s and 2.1 s, respectively), prolonged current stability (10^4 s and extrapolated to 10^9 s), and a low photo-/dark-current of approximately 10^{-8} and 10^{-11} A, which are favorable for low power-consumption photodetectors. The improvements in the supramolecular films can be attributed to their smooth and homogeneous morphologies, as well as fast charge-transfer kinetics, which ensure uniform carrier transport and counter-charge trapping, leading to efficient and stable photoinduced charge generation. This study reveals the potential functionality of host–guest interaction in enhancing the phototransistor's performance due to the size complementarity of ferrocene and β-CD, which preorganizes QD allocations in the supramolecular floating gate.

1. Introduction

Organic phototransistors are photo-activated sensors that convert light into electrical signals, and their three-electrode structure enhances light detection, offering benefits such as signal amplification and noise reduction.[1,2] The material systems used in phototransistor-based photodetectors typically consist of semiconductors and photoactive materials, which determine the charge transport properties and photoresponse of the device, respectively.[3] The various design approaches for photoactive layers using floating-gate dielectrics,[4–6] polymer electrets,[7,8] and ferroelectric electrets.[9] Floating-gate dielectrics comprise photoactive materials, such as perovskite nanocrystals, metal nanoparticles, fluorescent dyes, and quantum dots (QDs), dispersed

---

[a] Department of Materials Science and Engineering, National Taiwan University of Science and Technology, Taipei 10617, Taiwan. E-mail: lochentsyr@mail.ntust.edu.tw
[b] Department of Chemical Engineering, National Taiwan University, Taipei 10617, Taiwan. E-mail: chenwc@ntu.edu.tw
[c] Department of Chemical Engineering, Yuan Ze University, Taoyuan 320315, Taiwan
[d] Division of Applied Chemistry, Faculty of Engineering, Hokkaido University, Sapporo 060-8628, Japan
[e] List Sustainable Digital Transformation Catalyst Collaboration Research Platform (ICReDD List-PF), Institute for Chemical Reaction Design and Discovery, Hokkaido University, Sapporo 001-0021, Japan
[f] Department of Chemical & Materials Engineering, National Central University, Taoyuan 320317, Taiwan
[g] Department of Materials Science and Engineering, National Taiwan University, Taipei 10617, Taiwan
[h] Advanced Research Center of Green Materials Science and Technology, National Taiwan University, Taipei 10617, Taiwan
[i] Department of Chemical Engineering, National Cheng Kung University, Tainan 70101, Taiwan. E-mail: ycl@gs.ncku.edu.tw

† Electronic supplementary information (ESI) available. See DOI: https://doi.org/10.1039/d5tc01629k

within an insulating polymer matrix. This approach leverages the advantages of polymer materials while enhancing the performance of optoelectronic devices by incorporating light-absorbing materials.[10] Over the past decade, QD-based photonic devices have been developed with high figures of merit for various applications, including flexible imaging and biosensors, microelectronics, and up-conversion photodetectors, due to their tunable optoelectronic properties.[11] Therefore, QD floating-gate memory has been widely used in research related to optoelectronic devices.[12] For example, Jeong *et al.* reported that the surface engineering of CdSe QDs using small molecular ligands effectively promotes hole diffusion from the QDs to the conducting channel during the photoinduced recovery process, thereby reducing the erasing times. Notably, transistor memories incorporating a QD surface modified with fluorinated molecules exhibit nondestructive readout behavior. These memory devices exhibit high memory ratios of $>10^5$ for 10^4 s, along with good dynamic switching behavior during voltage-driven programming and light-assisted erasing processes within 1 s.[13]

According to related reports, hybrid perovskite nanocrystals have been modified with β-cyclodextrin (β-CD) to enhance their robustness and stability against environmental conditions and solvents during fiber production. These modified nanocrystals can be directly incorporated into organic semiconductors as charge-trapping units, improving charge dissociation and transport in semiconductor materials.[14] Notably, the functional groups of β-CD also facilitate the crystallization of perovskites, thereby aiding in the formation of uniform and large-area perovskite films. In supramolecular chemistry, a rapidly growing discipline that involves reversible bonding between components at the molecular scale, the typical non-covalent interactions include hydrophobic interactions, hydrogen bonding, host–guest interactions, π–π stacking, and electrostatic interactions.[15,16] In the case of charge-transfer interaction, Yang *et al.* reported a supramolecular electret memory device based on equimolar pyrene and 7,7,8,8-tetracyanoquinodimethane (TCNQ). Due to the favorable molecular association and dispersion between pyrene and TCNQ, the device exhibits excellent bistable switching behavior under both electrical and optical programming.[17] In addition, supramolecular gels comprising 1D C_{60} crystals are formed by controlling the dispersion of the antisolvent and C_{60} molecules. Photoelectric measurements have demonstrated that these C_{60} fibers exhibit outstanding photoresponse and exceptional detection performance.[18]

The design strategy of the host–guest supramolecular system involves a structurally complementary host and guest, where the guest fits into the host's binding pocket and is stabilized by non-covalent forces. This complementarity enables substrate specificity, while the weak host–guest attraction allows for reversible, non-invasive dissociation.[15] For example, Li *et al.* synthesized and studied three different monomers that self-assemble into linear supramolecular polymers (SLPs) *via* crown ether host–guest interactions. Upon introducing an additional monomer into the SLP solution, the SLP transforms into a cross-linked supramolecular polymer (SCP) through the host–guest interaction of the pillar arene group. This transformation enhances the fluorescence emission of SCP by suppressing electron transfer between the pillar arene and boron dipyrromethene groups.[19] Beyond applications in perovskite solar cells and light-emitting devices, this promising supramolecular host–guest inclusion strategy holds potential for various optoelectronic applications, including photodetectors, lasers, photocatalysis, and X-ray imaging.[20]

The host–guest structure between ferrocene and β-CD complexes has gained attention in supramolecular chemistry due to their enhanced properties and diverse applications. The combination of ferrocene's electrochemical activity and CD's unique ring structure enhances the electrochemical stability of Fc by reducing its solubility and increasing its retention at the electrode surface, thereby improving the reproducibility and robustness of the electrochemical process. Furthermore, these composites are facile and cost-effective, making them highly attractive for practical applications such as biosensors (*e.g.*, for detecting ascorbic acid) and food quality testing.[21,22] Recently, the incorporation of QDs into a ferrocene–CD complex (Fc–CD–QD) has emerged as a versatile approach. For example, Du *et al.* successfully developed polymeric hydrogels with electrochemical activity using the so-called ferrocene-HIC structure, where QDs coated with CD form the core and the ferrocene-ended copolymer serves as the shell. The resulting hydrogel, when heated above the lower critical solution temperature of poly(*N*-isopropylacrylamide), exhibited reversible sol–gel transitions as well as responsiveness to chemical oxidation and a guest molecule competing for ferrocene binding.[23]

By leveraging non-covalent interactions such as hydrogen bonding, π–π interactions, electrostatic forces, and hydrophobic interactions, these systems enable nuanced molecular assemblies that expand possibilities in material design and applications. However, research on the application of host–guest supramolecular systems in field-effect transistors and phototransistors remains relatively limited. Additionally, host–guest supramolecular interactions can facilitate the dispersion of QDs as floating gates, thereby enhancing the performance of optoelectronic transistors. However, among the above-mentioned non-covalent interactions, host–guest supramolecular systems are widely used in biomedicine but remain underexplored. Therefore, in this work, supramolecular floating-gate phototransistors based on the host–guest interaction between β-CD and poly(vinyl ferrocene) (PVFc) were investigated. Recently, considerable efforts have been devoted to enhancing the performance of perovskite photodetectors through structural and interfacial engineering strategies. For instance, Shafique *et al.* introduced Nb_2CT_x as a buried interface layer to passivate defects and improve carrier transport in self-powered photodetectors, achieving high responsivity and detectivity with suppressed dark current.[24] Meanwhile, Miao *et al.* designed gradient 2D–3D Ruddlesden–Popper perovskite films with vertically aligned phase distribution to accelerate vertical charge transport and achieve fast response, high detectivity, and long-term stability.[25] These findings underline the critical role of interfacial modulation and structural ordering in advancing perovskite optoelectronics. In this study, we propose a distinct supramolecular strategy involving β-CD-functionalized QDs and ferrocene-containing electrets to improve the charge trapping, dispersion, and operational durability of perovskite phototransistors. QDs were first modified with β-CD and subsequently dispersed in PVFc *via* supramolecular forces. The surface morphology of the host–guest composites was confirmed using an atomic force microscope (AFM). Time-resolved photoluminescence (TR-PL) spectroscopy was employed to characterize the charge transfer dynamics of the device by examining lifetime variations associated with defect states, which were further correlated with the electrical properties. Additionally, the modified QDs (CD@QD), which blended with polystyrene (PS) and lacked a structurally complementary feature, were utilized as a counterpart to verify the advantages of host–guest interaction in device performance. The CD@QD-PVFc device achieved long-term stable current retention and highly repeatable operation in photodetector applications.

2. Experimental section

2.1 Materials

Lead bromide ($PbBr_2$) (≥98%) was purchased from Tokyo Chemical Industry. Methylammonium bromide (MABr) was obtained from Greatcell Solar Materials. *N*-Octylamine (≥99%), β-CD, *N*,*N*-dimethylformamide (DMF, anhydrous ≥99%), toluene (anhydrous ≥99%), and chlorobenzene (anhydrous, 99%) were purchased from Sigma-Aldrich. The synthetic procedures for PVFc ($M_n = 2300$, $Đ = 1.17$) and PS ($M_n = 7400$, $Đ = 1.21$) were based on the previously reported methods.[36,37] The 2,9-dioctylanthra[2,1,9-*def*:6,5,10-*d″e″f″*] diisoquinoline-1,3,8,10(2*H*,9*H*)-tetraone (BPE-PDI) was obtained from Luminescence Technology Corp.

2.2 Preparation of perovskite nanocrystals

Perovskite precursor solutions were prepared at room temperature by dissolving 0.2 mmol of CH_3NH_3Br and 0.2 mmol of $PbBr_2$ in 0.5 mL of DMF, while 10 mg of β-CD was added in 0.4 mL of DMF. After obtaining a homogeneous and transparent solution, 30 μL of octylamine and 100 μL of the perovskite precursor solution were added to the β-CD solution. To form perovskite nanocrystals (CD@QD), 0.1 mL of the mixture was added to 50 mL of vigorously stirred toluene, and the color changed to green, emitting light under UV excitation simultaneously. The resulting solution was centrifuged at 9000 rpm for 10 minutes. After ultrasonic treatment, the solvent was removed using a rotary evaporator. The collected particles were dried under a vacuum overnight. The resulting powder was dispersed in chlorobenzene at a concentration of 5 mg mL^{-1} *via* ultrasonic treatment and stored in a nitrogen-filled glove box for further use.

2.3 Fabrication and characterization of phototransistors

First, CD@QD, PVFc, and PS were prepared at a concentration of 5 mg mL^{-1}. 2, 5, and 10 wt% of CD@QD were blended into an insulating polymer of PVFc, denoted as FcQD-1, FcQD-2, and FcQD-3, respectively. The mixture was stirred overnight in a nitrogen-filled glove box. The resulting solution was spin-coated onto a highly n-doped silicon wafer with a 300-nm-thick SiO_2 layer at 1000 rpm for 60 s under a nitrogen atmosphere. Notably, the substrate was pretreated with oxygen plasma to enhance its surface hydrophilicity. Subsequently, a 50-nm-thick BPE-PDI layer was thermally deposited onto the hybrid film under a vacuum of 10^{-7} Torr. Finally, gold contact electrodes (70 nm thick) were deposited onto the polymer film using a standard shadow mask, defining a channel width and length of 1000 and 50 μm, respectively. The optoelectronic properties of the photodetectors were characterized using a Keithley 2634B semiconductor parameter analyzer in a nitrogen-filled glove box. The I_{ds} of the transient photocurrent characterization was measured at $V_d = 100$ V. The transfer characteristics were obtained by sweeping the V_g from −40 to 100 V while maintaining a fixed V_d of 100 V. Dark current noise measurements were carried out using a Keithley 4200-SCS semiconductor parameter analyzer in a nitrogen-filled glove box.

2.4 Characterization

Morphological analysis of the CD@QD within the fabricated nanofiber was characterized using transmission electron microscopy (TEM, JEOL JEM-2100F). Surface morphology characterizations of pristine and blended films were performed using an AFM (Bruker Innova) operated in tapping mode. The film thickness was determined using an optical thickness measurement system (OPTMA3, Otsuka Electronics Co., Ltd). The silicon cantilevers (Nanosensor PPP-SEIHR) had a spring constant of 15 N m^{-1} and a resonant frequency of 320 kHz. UV-vis absorption spectra of the blended films were obtained using a Hitachi U-4100 spectrophotometer. The photoluminescence quantum yield (PLQY) was measured by LED device Analysis (Enli Technology LQ-100). TR-PL spectroscopy was conducted using an optical fiber coupled to a spectrometer (iHR320, HORIBA) and detected with a Hamamatsu C10910 streak camera, equipped with an M10913 slow single-sweep unit and a 375 nm pulsed laser, along with a delay generator (Stanford Research Systems DG645) at the National Synchrotron Radiation Research Center (NSRRC) in Taiwan. The field-effect mobility (μ) and threshold voltage (V_{th}) were calculated from a linear fit at the saturation regime according to the following equation:

$$I_{ds} = \mu \frac{W}{2L} C_{ox} \left(V_g - V_{th}\right)^2 \tag{1}$$

where C_{ox} is the combined areal capacitance of a 300-nm-thick SiO_2 layer (10.5 nF cm^{-2}).

3. Results and discussion

3.1 Structure of the phototransistors with host–guest supramolecules

PVFc is an electroactive polymer with ferrocene side groups attached to a vinyl polymer backbone, which impart unique electrochemical activity and excellent film-forming properties,[26,27] making it promising for enhancing device sensitivity. In contrast to traditional insulating polymers such as PS, PVFc is expected to exhibit rapid and distinct photoresponse, particularly in photo-induced charge trapping and release. To further enhance their potential in sensing applications, β-CD-modified QDs were incorporated into PVFc to construct a floating gate layer, utilizing the host–guest supramolecular interaction. CD@QD enhances the stability of polycrystalline thin films and improves the colloidal stability of nanocrystals through host–guest interactions. As shown in Fig. S1 (ESI†), the image presents the evenly dispersed CD@QD in acetone under 365-nm UV light excitation. Therefore, CD@QD exhibits significantly enhanced stability against environmental factors and solvents, maintaining their integrity during film fabrication.[28–31] As a charge-trapping component in floating-gate memory, CD@QD facilitates charge dissociation and enhances charge transfer between semiconductor materials.[14] Moreover, ferrocene can form an inclusion complex with β-CD due to host–guest interactions, preorganization, and size complementarity. The cyclic structure of β-CD provides a hydrophobic cavity that accommodates hydrophobic molecules, such as ferrocene. This size and shape complementarity enable ferrocene to be stably encapsulated within the β-CD cavity, forming a stable inclusion complex.[19,32] To prepare host–guest supramolecular films, the insulating polymer PVFc was mixed with CD@QDs at different weight ratios. The resulting solutions were spin-coated onto a plasma-treated silicon wafer to form the floating gate dielectric. Subsequently, an n-type semiconductor channel of BPE-PDI and the contact electrodes were thermally deposited for device fabrication. The chemical structure of the polymer, device structure, and schematic of host–guest interactions are shown in Fig. 1. The impact of the supramolecular system, designated as FcQD, on photodetector performance is further discussed in the following sections.

3.2 Optical and energy level properties of the host–guest supramolecules

Before studying the phototransistor sensor devices, it is essential to characterize the light absorption, photoluminescence (PL), and energy levels of the materials. Fig. 2(a) shows the UV-Vis absorption spectra of BPE-PDI, CD@QD, and FcQD. BPE-PDI exhibits a broad absorption range, covering the entire visible light spectrum. The absorption range of CD@QD and FcQD range from about 320 to 520 nm. It is worth noting that FcQD exhibits a slight blue shift compared to CD@QD, indicating the well-dispersed nature of the QDs in the supramolecular structure. Based on the absorption profiles of all constituent materials, which span from the UV to visible range, the phototransistor is expected to exhibit a panchromatic photoresponse. Further investigation of the steady-state PL spectra in Fig. 2(b) reveals that FcQD also exhibits a slight blue shift compared to the β-CD-modified QDs. This provides additional evidence that the supramolecular structure promotes uniform QD dispersion and inhibits aggregation from hydrogen bonding interactions between β-CDs.[33,34]

Next, the absorption onset of the studied material is used to evaluate the band gap (E_g). The cyclic voltammetry (CV) curves, shown in Fig. S2 (ESI†), indicate that PVFc possesses much stronger electroactive characteristics compared to PS. Combined with the onset of oxidation in the CV curve, the highest occupied molecular orbital (HOMO) and lowest unoccupied molecular orbital (LUMO) are determined by the equation of LUMO = HOMO + E_g. Fig. 2(c) summarizes the obtained energy levels, with the (LUMO, HOMO) levels of BPE-PDI, CD@QD, PVFc, and PS being (−4.3, −6.3) eV, (−3.9, −6.2) eV, (−0.5, −4.5) eV, and (−1.6, −7.0) eV, respectively. Notably, PVFc with higher HOMO/LUMO levels will facilitate hole transfer in the device, which is anticipated to improve the device stability with a supramolecular floating gate dielectric.

To gain insight into the charge transfer dynamics of the bilayered stack of supramolecules/BPE-PDI, TR-PL analysis was performed using 375-nm laser excitation. This analysis aimed to understand the effect of the supramolecular floating gate on

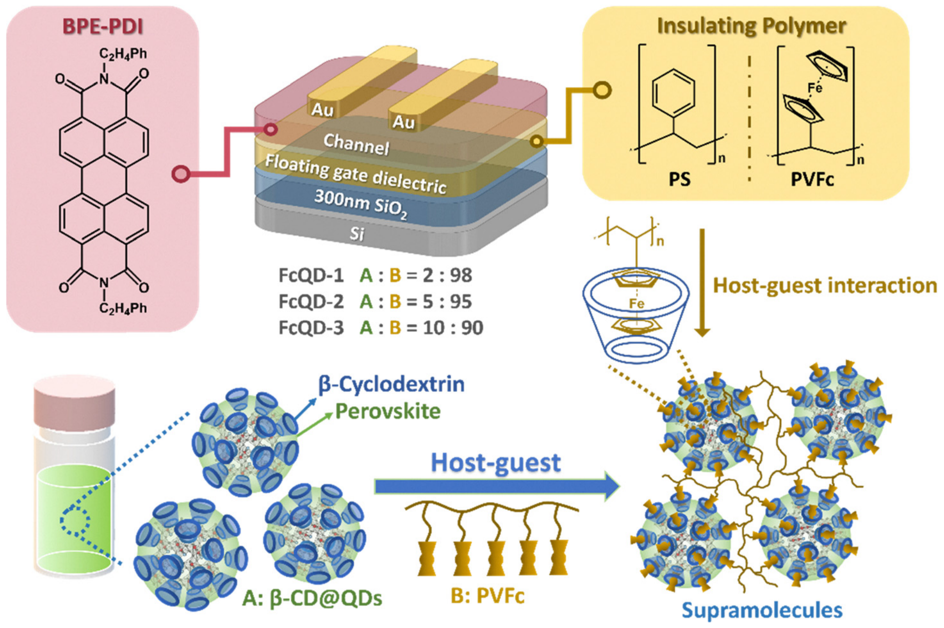

Fig. 1 Schematic illustration of the device structure, chemical structure, and supramolecular structure of an organic phototransistor incorporating the host–guest supramolecules comprising CD@QD-PVFc with their compositions in weight ratios.

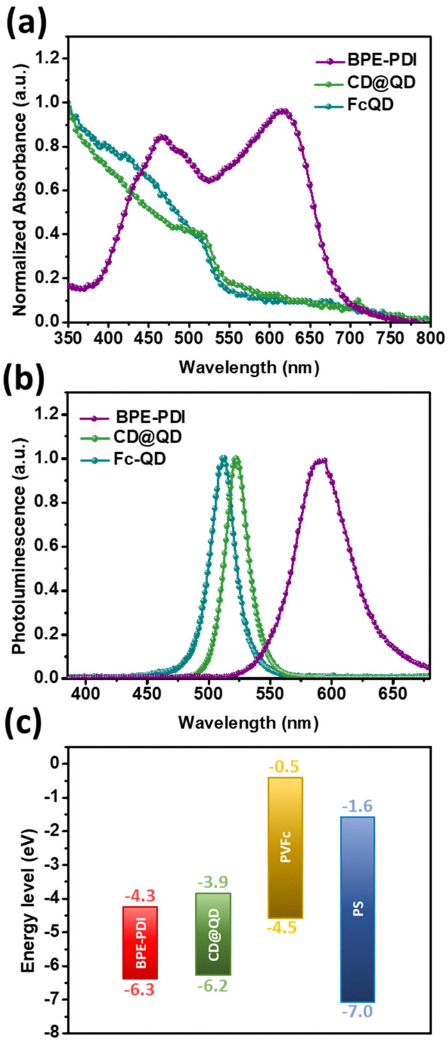

Fig. 2 (a) UV-vis absorption and (b) photoluminescence spectra of the Fc-QD, CD@QD, and BPE-PDI thin films. (c) The energy level diagram of the polymers, perovskite nanocrystal of CD@QD, and an electron-transport layer of BPE-PDI.

the photoresponse of the BPE-PDI channel. The 2D contour plots (Fig. 3(a) and Fig. S3b, ESI†) and 1D decay curves (Fig. 3(b) and Fig. S3c, ESI†) were fitted using a biexponential model, with the corresponding fitting parameters summarized in Table 1. The average exciton lifetime of BPE-PDI is 0.31 ns; however, in the presence of the CD@QD film, the exciton lifetime of BPE-PDI decreases to 0.22 ns, indicating poor exciton stability of the active layer and suggesting some hindrance to charge transport. In contrast, when BPE-PDI was deposited onto the FcQD films, the lifetimes of FcQD-1, FcQD-2, and FcQD-3 improved to 0.40, 0.39, and 0.32 ns, respectively, indicating fewer defects in the active layer, leading to enhanced stability. This result suggests that PVFc is an excellent matrix for dispersing the CD@QDs and avoiding the formation of structural defects in BPE-PDI.

3.3 Phototransistor performance of the host–guest supramolecules

In addition to photophysical properties, the morphology of the host–guest supramolecular films is also crucial for the device performance. TEM images of the β-CD-modified quantum dots (CD@QDs) and the FcQD-2 hybrid system are shown in Fig. 3(c) and (d). The CD@QDs exhibit relatively larger and less uniform particle sizes compared to those of FcQD-2. This observation suggests that the supramolecular interaction with PVFc contributes not only to improved dispersion stability but also to effective size refinement of the QDs in the hybrid system. Thus, AFM is used for morphological characterization of the CD@QDs dispersion within supramolecular structures. Fig. 3(e)–(h) shows the AFM images of PVFc and CD@QD-PVFc films with different mixing ratios. The lower part of each image displays the topography after BPE-PDI deposition. The morphology of the pure BPE-PDI is shown in Fig. S3a (ESI†). As can be seen, upon incorporating CD@QD into PVFc, the surface roughness decreased, stabilizing at 0.4 to 0.5 nm. After the deposition of BPE-PDI, the films exhibit similar morphologies between different blending ratios. These results suggest that the CD@QDs are well dispersed due to the complementary structure between β-CD and PVFc, as no apparent QD aggregation is observed on the surface. Therefore, the blending ratio has no interference in the formation of the BPE-PDI channel layer.

After studying the optical and morphological properties of the hybrid films, their phototransistor applications were further explored. The device was designed with host–guest supramolecules as floating gate dielectrics and BPE-PDI as the channel material, fabricated on a SiO_2 dielectric layer. The device architecture is shown in Fig. 1 and the fabrication procedure is detailed in the Experimental Section. The thicknesses of the pristine and composite floating gate films were measured using an optical thickness meter. The results show that the thicknesses of the PVFc and CD@QD pristine films are 18.5 nm and 82.4 nm, respectively. After blending CD@QDs with PVFc, the hybrid films exhibit thicknesses of 20.3 nm (FcQD-1), 20.9 nm (FcQD-2), and 24.6 nm (FcQD-3). These thicknesses fall within a suitable range for floating-gate dielectric layers in phototransistor devices, ensuring efficient charge trapping while maintaining reliable gate coupling. The electrical characterization of the photodetector was conducted by measuring its transfer characteristics under both dark and illuminated conditions (405 nm, 16.96 mW cm^{-2}). Fig. 4(d) and Fig. S4a–c (ESI†) display the transfer curves of devices utilizing FcQD-2, PVFc, FcQD-1, and FcQD-3 as photosensing layers, respectively, all of which exhibit typical n-type transport behavior. The transfer curves were obtained by sweeping the gate voltage (V_g) from −40 to 100 V at a fixed drain voltage (V_d) of 100 V. The electrical performance of the phototransistors was evaluated under dark conditions, and the transfer curves for devices based on the PVFc and FcQD composites are shown in Fig. 4(d) and Fig. S4a–c (ESI†). As shown in Table 2, the electron mobilities (μ_e) under dark conditions for PVFc, FcQD-1, FcQD-2, and FcQD-3 are 3.51×10^{-3}, 2.02×10^{-3}, 1.06×10^{-3}, and 8.04×10^{-4} $cm^2\ V^{-1}\ s^{-1}$, respectively. The results indicate a decreasing trend in mobility with increasing QD content, suggesting that excessive QD loading may hinder charge transport due to increased trap density or disrupted polymer matrix continuity. To evaluate the effect of mild thermal processing on charge

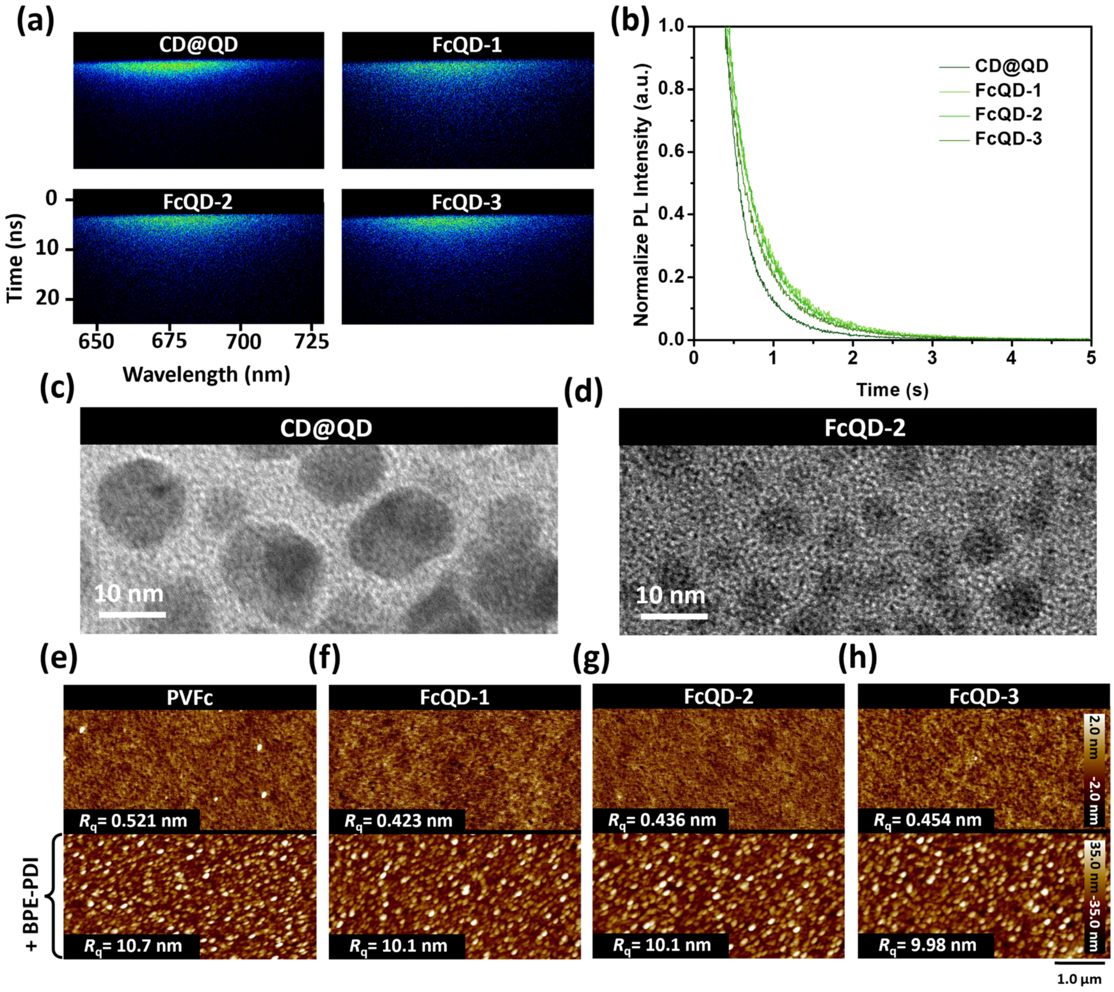

Fig. 3 (a) TR-PL 2D contour plots and (b) the corresponding 1D decay profiles of the bilayered films (FcQD/BPE-PDI) under 375-nm laser excitation. TEM image of (c) β-CD-modified quantum dots (CD@QD) and (d) the FcQD-2 hybrid system. (e)–(h) AFM height images of PVFc and CD@QD-PVFc films with different blending ratios (top) and the bilayered films deposited with BPE-PDI (bottom).

Table 1 Summary of the optical parameters of host–guest supramolecules. Note that all samples in this table have been deposited with BPE-PDI small molecules

Sample	PLQY[a] (%)	A_1[b] (%)	τ_1[b] (ns)	A_2[b] (%)	τ_2[b] (ns)	τ_{avg}[c] (ns)
BPE-PDI	13.61	2.71	1.16	97.29	0.29	0.31
CD@QD	11.74	8.06	0.57	91.94	0.19	0.22
FcQD-1	11.62	24.07	0.72	75.93	0.30	0.40
FcQD-2	11.37	11.86	0.84	88.14	0.33	0.39
FcQD-3	11.58	20.63	0.62	79.37	0.24	0.32

[a] Photoluminescence quantum yield excited by a 365-nm light source. [b] Biexponential function: $I_f(t) = A_1\exp(-t/\tau_1) + A_2\exp(-t/\tau_2)$, where $I_f(t)$ is the fluorescence intensity, A_1 and A_2 are the scaling constant, t is the fluorescent decay time, and τ_1 and τ_2 are the fitted time constants, respectively. The TRPL measurement was conducted with a 375-nm laser. [c] The averaged lifetime (τ_{avg}) is calculated by $\tau_{avg} = (A_1 \times \tau_1^2 + A_2 \times \tau_2^2)/(A_1 \times \tau_1 + A_2 \times \tau_2)$.

transport, thermal annealing at 60 °C for 30 minutes was applied to the supramolecular CD@QD floating gate layer. Interestingly, the device without thermal treatment exhibited a higher mobility of 1.51×10^{-3} cm^2 V^{-1} s^{-1} than that of 1.20×10^{-3} cm^2 V^{-1} s^{-1} after annealing. This result suggests that in the CD@QD system, where host–guest interactions and supramolecular forces govern the dispersion and interfacial stability of QDs, additional thermal energy may disrupt the optimized assembly or induce partial aggregation. As a result, thermal annealing does not further enhance, and may even compromise, the dispersion state that is critical for efficient charge modulation. Therefore, no post-deposition thermal treatment was adopted in our optimized fabrication process. Fig. S5 (ESI†) presents the transfer characteristics of the CD@QD phototransistor after thermal treatment at 60 °C. The measurements were performed under dark conditions at V_d = 100 V.

To evaluate the device's temporal response, the photodetector was illuminated with 405-nm light by sweeping V_d from 0 to 100 V at V_g = 0 V. The resulting output characteristics of these devices are shown in Fig. S6a–d (ESI†). Since rapid response upon signal detection is a critical requirement for high-performance sensing systems, the response dynamics, depicted in Fig. 4(a) and Fig. S4d–f (ESI†), were measured at a horizontal bias of 100 V. The rise time (t_r) and fall time (t_f) were defined as

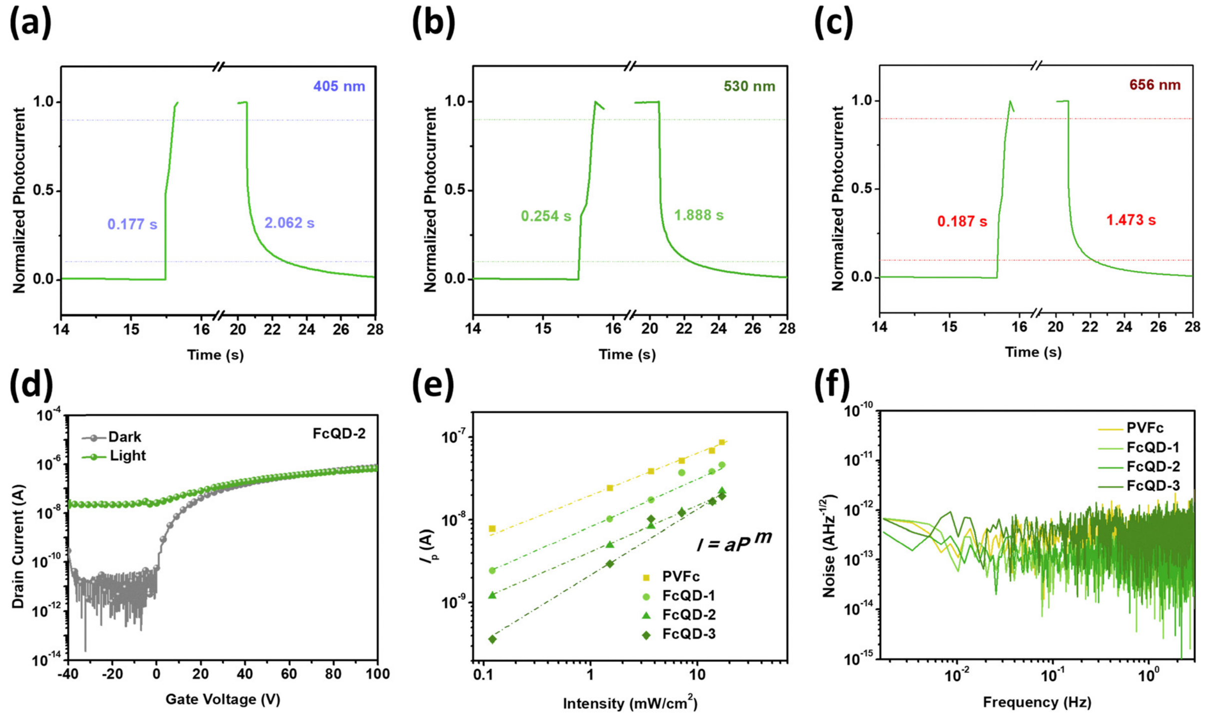

Fig. 4 (a)–(c) Transient photocurrent characteristics of the FcQD-2 device under illumination of (a) 405, (b) 530, and (c) 656-nm light for 5 s. (d) Transfer curves of the FcQD-2 device in the dark and under illumination at 405 nm. Note that the drain currents in (a)–(d) were measured at V_d = 100 V under a light intensity of 16.96 mW cm^{-2}. (e) The relationship between photoresponse current and irradiance, along with the fitted lines based on the equation of $I = aP^m$. (f) Dark current noise measurement of CD@QD-PVFc photodetectors.

the time required for the photocurrent (I_p) to increase from 10% to 90% and decrease from 90% to 10%, respectively. The calculated results are summarized in Table 2. The measured (t_r, t_f) values for PVFc, FcQD-1, FcQD-2, and FcQD-3 were (0.477, 3.765) s, (0.423, 2.950) s, (0.177, 2.389) s, and (0.142, 2.414) s, respectively. The enhanced response characteristics can be attributed to the improved grain size uniformity and reduced surface roughness, as observed in the AFM images. A smoother surface minimizes charge trapping and facilitates more efficient charge transport during light programming. Among all the devices, the FcQD-2 photodetector exhibited the best electrical performance, highlighting the potential of host–guest supramolecules in the development of advanced optical sensing devices.

The relationship between I_p and irradiance was analyzed to understand the effect of defect passivation by host–guest supramolecules on the photodetector performance. Six different light intensities, ranging from 0.12 to 16.96 mW cm^{-2}, were utilized to illuminate the FcQD-2 device, as shown in Fig. 4(e). To gain further insight into its photoresponse, the curves were fitted using the following equation:

$$I = aP^m \tag{2}$$

where I and P represent the current and irradiance, respectively, while a and m denote the fitting factor and exponent, respectively. The fitted m values for PVFc, FcQD-1, FcQD-2, and FcQD-3 are 0.857, 0.838, 0.825, and 0.870, respectively. An ideal photodetector exhibits an m value of 1, indicating a trap-free environment with a direct proportionality between photoexcitation and carrier generation. The fitted values for all samples, though slightly below unity, suggest limited charge trapping. This can be attributed to the smooth and uniform film surface observed in the AFM results. Additionally, Fig. S7a (ESI†) is presented to investigate the relationship between photoresponsivity (R) and irradiance (0.12–16.96 mW cm^{-2}). R is determined

Table 2 Summary of the photodetector parameters based on the CD@QD-PVFc floating gate dielectric and BPE-PDI channel

Sample	μ_e (cm^2 V^{-1} s^{-1})	I_p[a] (A)	t_r[b] (s)	t_f[b] (s)	R[c] (A W^{-1})	I_n[d] (A Hz$^{-1/2}$)	NEP[e] (W Hz$^{-1/2}$)	D*[f] (Jones)
PVFc	3.51×10^{-3}	8.63×10^{-8}	0.477	3.765	2.04×10^{-2}	1.74×10^{-13}	8.55×10^{-12}	1.85×10^{9}
FcQD-1	2.02×10^{-3}	4.63×10^{-8}	0.423	2.950	6.34×10^{-3}	1.40×10^{-13}	2.21×10^{-11}	7.16×10^{8}
FcQD-2	1.06×10^{-3}	2.22×10^{-8}	0.177	2.389	3.04×10^{-3}	1.47×10^{-13}	4.83×10^{-11}	3.27×10^{8}
FcQD-3	8.04×10^{-4}	1.93×10^{-8}	0.142	2.414	2.64×10^{-3}	2.78×10^{-13}	1.05×10^{-10}	1.50×10^{8}

[a] Saturated photocurrent under a V_d of 100 V and irradiance of 16.96 mW cm^{-2}. [b] Photocurrent rise time and fall time defined by the time elapsed between 10% and 90% saturated photocurrent. [c] Photoresponsivity: $R = I_p/PA$. [d] Dark current noise measured at 1 Hz. [e] Noise equivalent power: NEP = I_n/R. [f] Specific detectivity according to the 405-nm light illumination and the dark current noise measured at 1 Hz.

using eqn (2), and the calculated values under 16.96 mW $\mathrm{cm^{-2}}$ irradiation are summarized in Table 2.

$$R = I_\mathrm{p}/PA \quad (3)$$

where P and A represent the irradiance and the illuminated area, respectively. The calculated R values are all on the order of 10^{-2} to 10^{-3}, which are consistent with the results presented in Fig. 4(e). The external quantum efficiency (EQE) was further calculated to evaluate the photoelectric conversion efficiency of the phototransistors. EQE was determined based on the following equation: EQE = $(R \times h \times c)/(e \times \lambda)$, where h is the Planck constant, c is the speed of light, e is the elementary charge, and λ is the wavelength of incident light, 405 nm. Based on this calculation, the EQEs of PVFc, FcQD-1, FcQD-2, and FcQD-3 were 6.26%, 1.95%, 0.93%, and 0.81%, respectively. While R is used to evaluate the device's responsiveness to optical signals, detectivity reflects its sensitivity to weak incident light. Fig. 4(f) presents the dark noise spectral density (I_sd) of the photodetector at various frequencies. As shown in Table 2 and Fig. S7b (ESI†), the I_sd values of PVFc, FcQD-1, FcQD-2, and FcQD-3 at 1 Hz fall within the low current noise range of 10^{-2} to 10^{-3} A $\mathrm{Hz^{-1/2}}$. The specific detectivity (D^*) is defined using the following equation:

$$D^* = (Af)^{1/2}/\mathrm{NEP} \quad (4)$$

where f is the bandwidth, and NEP (noise equivalent power) is defined as NEP = I_sd/R. The devices exhibit low noise characteristics and high D^*s, which range from 10^8–10^9 Jones for the phototransistors, indicating excellent light-sensing performance based on the supramolecules.

Based on the UV-visible absorption spectrum, the investigated devices exhibit a panchromatic photoresponse. Therefore, transient photocurrent measurements using FcQD-2 were performed under various light sources (405, 530, and 656 nm) to evaluate the multicolor and broadband responsivity, as shown in Fig. 4(a)–(c). Notably, the response time varied under different wavelengths of illumination. As can be seen, when exposed to 405 nm light, the device exhibited a relatively short t_r value. This difference is attributed to spectral absorption differences. While all three wavelengths can excite BPE-PDI, the enhanced response rate observed at 405 nm is attributed to the additional excitation of QDs, which absorb strongly in the same region and contribute to more efficient photoinduced charge generation. Moreover, FcQD-2 demonstrates superior performance compared to PVFc (Fig. S4, ESI†), exhibiting improved charge retention and faster response times, which highlights the importance of host–guest structure design. The incorporation of QDs enhances the surface morphology and charge transport, leading to higher sensitivity and better broadband detectivity, which make FcQD-2 a more efficient and stable material for photodetector and other optoelectronic applications.

3.4 Long-term durability of the phototransistors

Long-term stability and endurance are crucial factors for real-life applications. As a result, to evaluate the stability and switching durability of the photodetectors, long-term retention tests were conducted, as shown in Fig. 5(a) and (b) for FcQD-2 and PVFc, respectively. The results indicate that FcQD-2, which incorporates QDs, exhibits highly stable light and dark state currents under continuous illumination and in the absence of light for 3×10^4 s. With extrapolation, the dark current stability can be maintained over 10^4 to 10^9 s. In contrast, PVFc, being an electrochemically active material, exhibits significant instability in dark conditions. In the absence of QDs, extended voltage stress results in current fluctuations probably due to the electroactive nature and instability of PVFc, which significantly compromises the detector's reliability. In addition to retention measurements, cyclic photoresponse tests were performed under ambient conditions (room temperature, nitrogen environment) to evaluate operational stability. Devices based on CD@QDs and FcQD-2 were subjected to 10 consecutive cycles of alternating 5-second illumination and 5-second dark intervals. As shown in Fig. S8 (ESI†), compared to the control device (CD@QDs only), the device incorporating PVFc (Fig. 5(c)) exhibits significantly improved photoresponse stability, with minimal hysteresis and consistent photocurrent levels throughout the cycles. In contrast, the CD@QD-only device displays pronounced hysteresis and a gradual increase in drain current during repeated cycling, suggesting unstable charge trapping and incomplete recovery under dark conditions. These results confirm that the incorporation of PVFc not only enhances the initial performance but also improves operational durability under repeated switching, attributed to the charge-buffering role of the ferrocene units within the supramolecular floating gate. Additionally, as shown in Fig. 5(c), FcQD-2 maintains a stable switching capability even after 100 cycles of repeated switching operations, demonstrating the robustness of FcQD host–guest supramolecular systems. This enhanced stability ensures reliable phototransistor performance without compromising device functionality.

3.5 Operating mechanism of the phototransistors comprising supramolecules

To corroborate the device mechanism, a reference device comprising the CD@QD-PS system (PSQD) was developed and characterized. PSQD lacks structural complementarity and was evaluated to highlight the significance of host–guest interaction in the floating gate for enhancing the electrical properties of optoelectronic devices. The AFM images of PS and PSQD, shown in Fig. S9a and b (ESI†), reveal similar surface roughness of around 0.4–0.5 nm. The TR-PL 2D images (Fig. S9c, ESI†) and 1D decay curves (Fig. S9d, ESI†) were fitted with a biexponential model, and the corresponding parameters are summarized in Table S1 (ESI†) and upon incorporating CD@QDs into PS, the exciton lifetime of BPE-PDI decreased, indicating an increase in defect density. These results suggest that defect formation in the PSQD device may deteriorate the photodetector's performance. Concerning the device influence, first, PS is used as a polymer electret, and PSQD serves as a floating gate in the control group. Fig. 6(a) and Fig. S10a, b (ESI†) show the transfer and output curves of devices with PS, PSQD, and CD@QD as the floating gate dielectrics. All of which exhibit typical n-type device characteristics. The response dynamics shown in Fig. 6(b) were measured at V_d = 100 V. When PS was used as

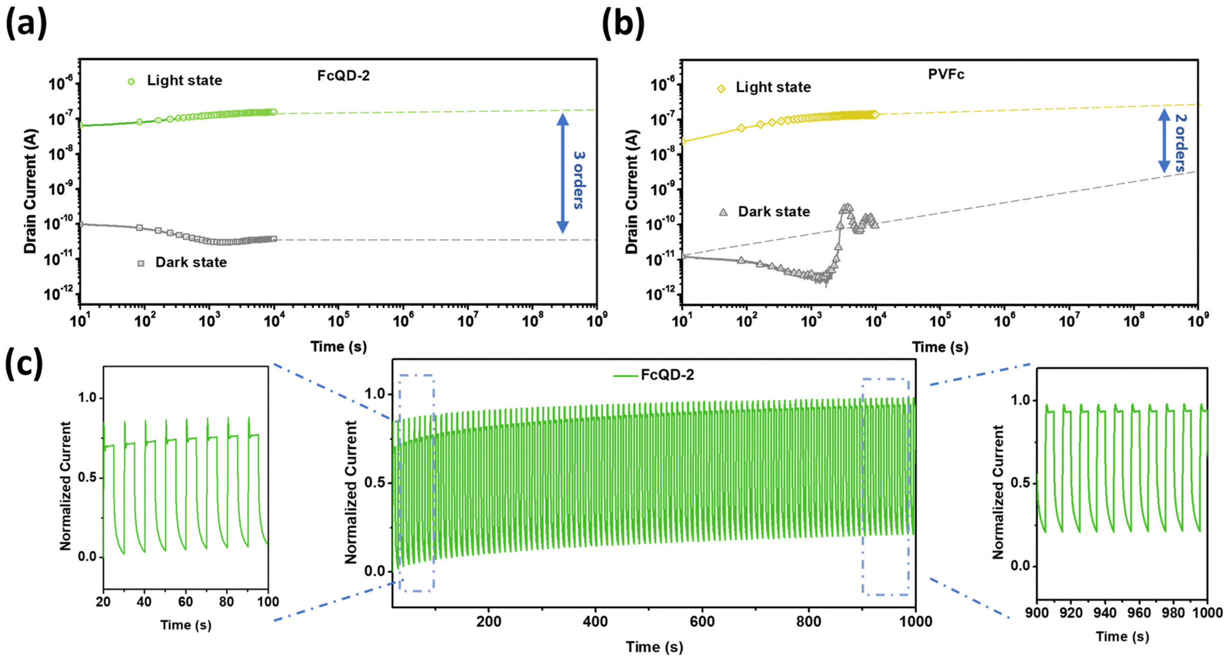

Fig. 5 (a) and (b) Long-term stability of devices based on (a) FcQD-2 and (b) PVFc film under irradiation or in the dark. The drain current was recorded for 3×10^4 s, and the dotted line represents the 10-year long-term extrapolation. (c) Endurance test of the FcQD-2 photodetector, consisting of 100 cycles with 5 s of irradiation followed by 5 s of dark conditions. The images on either side indicate the start and end of the switching cycle. Note that the operating parameters in this figure are V_d = 100 V and 405-nm light (16.96 mW cm^{-2}).

an electret, the device showed a weak photoresponse with severe hysteresis. The reference device of PSQD behaves similarly to PS, exhibiting hysteresis, which is detrimental to phototransistor applications. In the case of CD@QD, since the

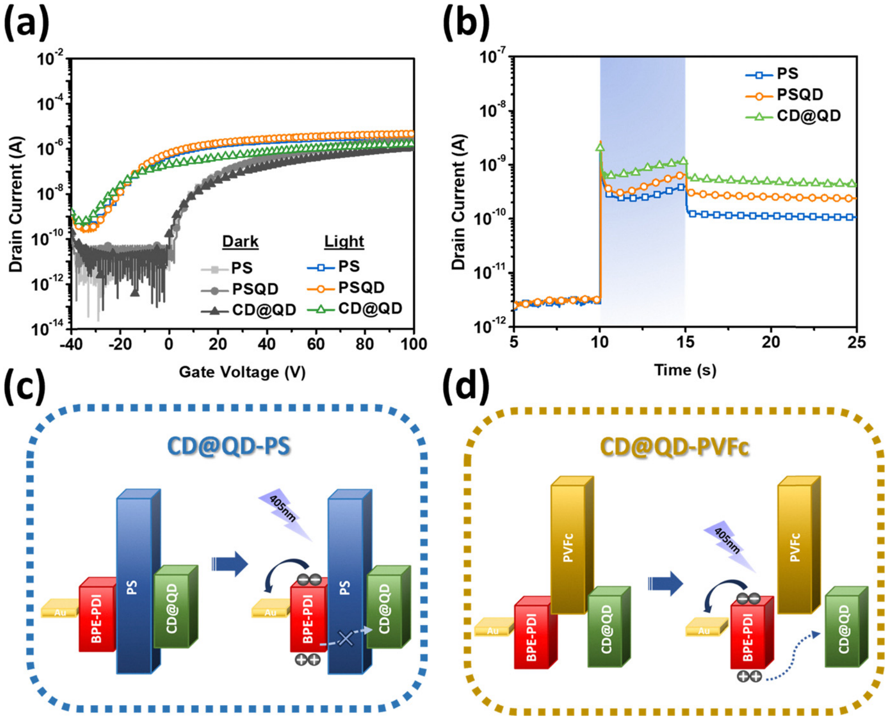

Fig. 6 (a) Transfer and (b) transient characteristics of the reference phototransistor devices. The drain current was measured at V_d = 100 V, and illumination was performed using 405-nm light (16.96 mW cm^{-2}; 5 s). Schematic illustrations of the working mechanisms for (c) CD@QD-PS and (d) CD@QD-PVFc phototransistor devices.

energy levels of CD@QD are closely aligned with those of BPE-PDI, charge storage behavior is still observed. Therefore, plausible device working mechanisms are proposed in Fig. 6(c) and (d) for devices based on PSQD and FcQD, respectively. First, the HOMO level of PS is lower than those of both BPE-PDI and CD@QD, which acts as a barrier layer and hinders hole transfer after photoexcitation, which enhances the hysteresis and presents low photoresponse. In contrast, PVFc possesses a relatively high HOMO level, which facilitates the charge transfer and contributes to the rapid photoresponse. Upon 405 nm illumination, photogenerated carriers are primarily generated in the BPE-PDI semiconductor layer. Due to the favorable energy-level alignment between BPE-PDI and the CD@QD-PVFc floating gate, photogenerated holes can be transferred or tunnel through the interfacial barrier and become temporarily trapped in the supramolecular electret. This modulates the local electric field and effectively alters the channel conductivity. The dynamic trapping and de-trapping processes thus enable reversible photocurrent switching, contributing to the observed threshold shift and enhanced device response. We highlight the contrast between the PSQD and FcQD systems to distinguish the operation mechanisms further. As shown in Fig. S11 (ESI†), the PSQD-based device exhibits a distinct memory effect. The photocurrent increases under 405 nm illumination and remains elevated until an external gate bias (V_g = 100 V) is applied to erase the stored charges, confirming its charge retention capability and classification as a phototransistor memory. In contrast, the FcQD-based device is designed and operated as a photodetector, exhibiting reversible photoresponse behavior. Upon illumination, the drain current increases due to photocarrier generation and returns to its original level after the light is turned off, indicating no nonvolatile charge retention or memory behavior. These observations indicate that PSQD functions as a nonvolatile memory device, whereas FcQD offers a stable and repeatable photoresponse enabled by the supramolecular electret design. Like hybrid systems that rely on interfacial band alignment to enhance carrier separation, our supramolecular CD@QD design facilitates charge modulation through host–guest interactions and energy-level alignment. Abbas *et al.* reported that integrating perovskite QDs into junction architectures enhances the built-in electric field, supporting efficient carrier separation and improved device performance.[35] Notably, the host–guest interaction in FcQD further enhances the device's photoresponse and long-term stability due to the size complementarity of ferrocene and β-CD, which facilitates the preorganization of the homogeneous dispersion of CD@QD in the supramolecules.

4. Conclusion

In summary, an electroactive floating-gate memory layer was designed by utilizing host–guest supramolecular interactions between β-CD and ferrocene, resulting in a well-defined supramolecular structure. In the device architecture, the electroactivity of the polymer electret helps mitigate excessive charge accumulation, thereby contributing to the fast response characteristics. Furthermore, the incorporation of QDs significantly reduces the response time, especially in FcQD-2, which exhibits shorter rise and fall times, reflecting enhanced charge transport dynamics and reduced charge trapping. The reduced surface roughness (0.4–0.5 nm), as observed in AFM measurements, further supports the improved uniformity of the hybrid films, leading to more efficient charge transfer. Additionally, transient photocurrent measurements demonstrated that FcQD-2 exhibited superior broadband photoresponsivity, validating the effectiveness of the host–guest supramolecular structure in optimizing photodetector performance. These fast dynamics are in good agreement with the TRPL exciton lifetimes of the BPE-PDI channel. In addition, the combination of PVFc with other nanomaterials, including QDs and other functionalized polymers, presents exciting prospects for advancing photodetector and memory device technologies. The incorporation of QDs not only enhances the photoelectric conversion efficiency but also opens possibilities for tuning the device's response to specific wavelengths of light. This study underscores the potential of electroactive host–guest supramolecular memory layers in achieving high-performance phototransistors with enhanced photoresponse, stability, and charge retention. By leveraging the unique properties of PVFc, these devices are poised to revolutionize the field of optoelectronics, offering new solutions for applications ranging from photodetectors to advanced memory systems.

Author contributions

Yi-Wen Chen: investigation, writing original draft; Ya-Shuan Wu: data curation, methodology, manuscript reviewing & editing; Ender Ercan: quantum dots synthesis, validation; Takuya Isono: polymer synthesis and characterization; Toshifumi Satoh: polymer design; Cheng-Liang Liu: supervision; Yan-Cheng Lin: conceptualization, formal analysis; manuscript reviewing & editing; Chen-Tsyr Lo: visualization, supervision; Wen-Chang Chen: funding acquisition, resources, project administration. All authors read and approved the final manuscript.

Conflicts of interest

The authors declare that they have no conflict of interest.

Data availability

Data is available on request from the corresponding authors.

Acknowledgements

The authors appreciate the financial support from the Ministry of Education's Higher Education Sprout Project under the Featured Area Research Center Program (113L9006) and the National Science and Technology Council in Taiwan (NSTC 113-2221-E-002-062-MY3). Y.-C. L. also thanks the financial support from the

NSTC (113-2221-E-006-013-MY3). The authors also thank Dr Bi-Hsuan Lin for assisting with the TRPL measurements.

References

1 K. J. Baeg, M. Binda, D. Natali, M. Caironi and Y. Y. Noh, *Adv. Mater.*, 2013, **25**, 4267–4295.

2 C. Xie, C.-K. Liu, H.-L. Loi and F. Yan, *Adv. Funct. Mater.*, 2020, **30**, 1903907.

3 Y. C. Lin, W. C. Yang, Y. C. Chiang and W. C. Chen, *Small Sci.*, 2022, **2**, 2100109.

4 M. Carroli, A. G. Dixon, M. Herder, E. Pavlica, S. Hecht, G. Bratina, E. Orgiu and P. Samorì, *Adv. Mater.*, 2021, **33**, 2007965.

5 J. Pei, X. Wu, W. J. Liu, D. W. Zhang and S. J. Ding, *ACS Nano*, 2022, **16**, 2442–2451.

6 A. Tavasli, B. Gurunlu, D. Gunturkun, R. Isci and S. Faraji, *Electronics*, 2022, **11**, 316.

7 H. A. Lin, Y. H. Weng, T. Mulia, C. L. Liu, Y. C. Lin, Y. Y. Yu and W. C. Chen, *ACS Appl. Mater. Interfaces*, 2024, **16**, 25042–25052.

8 T. Mulia, E. Eran, M. Mumtaz, Y. C. Lin, R. Borsali and W. C. Chen, *Carbohydr. Polym.*, 2024, **344**, 122476.

9 S. Han, T. Ma, H. Li, J. Wu, R. Liu, R. Cao, F. Li, H. Li and C. Chen, *Adv. Funct. Mater.*, 2024, **34**, 2309910.

10 S.-T. Chang, W.-C. Chen, C.-F. Lin, P.-Z. Yu, C.-H. Tsai, C.-J. Cho, Y.-C. Lin, W.-C. Chen and C.-C. Kuo, *Adv. Opt. Mater.*, 2024, **12**, 2400470.

11 J. Kim, S. Song, Y. H. Kim and S. K. Park, *Small Struct.*, 2021, **2**, 2000024.

12 C.-H. Tsai, W.-C. Chen, Y.-C. Lin, Y.-H. Huang, K.-W. Lin, J.-Y. Wu, T. Satoh, W.-C. Chen and C.-C. Kuo, *Small*, 2024, **20**, 2402567.

13 Y. J. Jeong, D. J. Yun, S. H. Noh, C. E. Park and J. Jang, *ACS Nano*, 2018, **12**, 7701–7709.

14 E. Ercan, Y.-C. Lin, L.-C. Hsu, C.-K. Chen and W.-C. Chen, *Adv. Mater. Technol.*, 2021, **6**, 2100080.

15 Y. Liu, Y. Wu, Z. Luo and M. Li, *iScience*, 2023, **26**, 106279.

16 G. T. Williams, C. J. E. Haynes, M. Fares, C. Caltagirone, J. R. Hiscock and P. A. Gale, *Chem. Soc. Rev.*, 2021, **50**, 2737–2763.

17 Y.-F. Yang, Y.-C. Chiang, Y.-C. Lin, G.-S. Li, C.-C. Hung and W.-C. Chen, *Adv. Funct. Mater.*, 2021, **31**, 2102174.

18 K. Liu, S. Gao, Z. Zheng, X. Deng, S. Mukherjee, S. Wang, H. Xu, J. Wang, J. Liu, T. Zhai and Y. Fang, *Adv. Mater.*, 2019, **31**, 1808254.

19 H. Li, Z. Huang, X. Huang, W. Huang, S. Rao, S. Liu, Y. Zhang and W. Tian, *Macromolecules*, 2024, **57**, 1328–1336.

20 H. Chen, X. Chang, G. Yang, B.-X. Lei and W.-Q. Wu, *Microstructures*, 2024, **4**, 2024031.

21 G. Zhang, X. Wang, X. Shi and T. Sun, *Talanta*, 2000, **51**, 1019–1025.

22 S. Takahashi and J. i Anzai, *Materials*, 2013, **6**, 5742–5762.

23 P. Du, J. Liu, G. Chen and M. Jiang, *Langmuir*, 2011, **27**, 9602–9608.

24 S. Shafique, A. Qadir, T. Iqbal, M. Sulaman, L. Yang, Y. Hou, Y. Hou, Y. Miao, J. Wu, Y. Wang, F. Zheng, X. Wang and Z. Hu, *J. Alloys Compd.*, 2024, **1004**, 175903.

25 Y. Miao, J. Wu, X. Qi, L. Yang, X. Wang, F. Zheng, F. Zhao, S. Shafique, Y. Zhu and Z. Hu, *Nano Energy*, 2023, **113**, 108605.

26 H. Ju and D. Leech, *J. Chem. Soc., Faraday Trans.*, 1997, **93**, 1371–1377.

27 R. Candeago, H. Wang, M. T. Nguyen, M. Doucet, V. A. Glezakou, J. F. Browning and X. Su, *JACS Au*, 2024, **4**, 919–929.

28 D. Wei, H. Huang, P. Cui, J. Ji, S. Dou, E. Jia, S. Sajid, M. Cui, L. Chu, Y. Li, B. Jiang and M. Li, *Nanoscale*, 2019, **11**, 1228–1235.

29 S. Masi, F. Aiello, A. Listorti, F. Balzano, D. Altamura, C. Giannini, R. Caliandro, G. Uccello-Barretta, A. Rizzo and S. Colella, *Chem. Sci.*, 2018, **9**, 3200–3208.

30 S. Huang, T. Zhang, C. Jiang, R. Qi, C. Luo, Y. Chen, H. Lin, J. Travas-sejdic and H. Peng, *ChemNanoMat*, 2019, **5**, 1311–1316.

31 F. Guo, Y.-Y. Wang, J. Zhang, X.-L. Wei and Z.-H. Mo, *New J. Chem.*, 2020, **44**, 17368–17373.

32 A. Harada and S. Takahashi, *J. Chem. Soc., Chem. Commun.*, 1990, 1322–1323.

33 K. McGuire, S. He, J. Gracie, C. Bryson, D. Zheng, A. W. Clark, J. Koehnke, D. J. France, W. M. Nau, T.-C. Lee and W. J. Peveler, *ACS Nano*, 2023, **17**, 21585–21594.

34 D. Dorokhin, N. Tomczak, M. Han, D. N. Reinhoudt, A. H. Velders and G. J. Vancso, *ACS Nano*, 2009, **3**, 661–667.

35 K. Abbas, P. Ji, N. Ullah, S. Shafique, Z. Zhang, M. F. Ameer, S. Qin and S. Yang, *Microsyst. Nanoeng.*, 2024, **10**, 81.

36 S. Katsuhara, H. Mamiya, T. Yamamoto, K. Tajima, T. Isono and T. Satoh, *Polym. Chem.*, 2020, **11**, 2995–3002.

37 Y.-C. Chen, Y.-C. Lin, H.-C. Hsieh, L.-C. Hsu, W.-C. Yang, T. Isono, T. Satoh and W.-C. Chen, *J. Mater. Chem. C*, 2021, **9**, 1259–1268.